4.4. Conclusions

The Sandia/Michigan EIT system and reconstruction algorithm have been validated for the quantitative measurement of solid volume fractions in solid-liquid flows and gas volume fractions and radial profiles in gas-liquid flows. EIT was used to measure solid volume fractions of up to 0.05, with excellent agreement between EIT results and the nominal values determined from the known mass of solids in each flow. Gas-liquid bubble-column flows were measured simultaneously with EIT and GDT; for cross-sectionally-averaged gas volume fractions up to 0.15 the average values and radial profiles from EIT and GDT agreed to within 0.01, despite large radial variations across the column.

As demonstrated through the "phantom" validations in Chapter 3 and the two-phase tests in this chapter, the EIT hardware and reconstruction algorithm have the ability to reproduce parabolic gas volume fraction distributions and the size and location of an insulating cylinder centered off the domain axis. With the recent addition of quartic conductivity profiles to the reconstruction library, the EIT system can also be applied to the study of the effects of solids on vertical churn-turbulent column flows. Two-phase tests employing both GDT and EIT indicate that the quartic terms in both methods have about the same importance. A slight modification of the Maxwell-Hewitt relation, also suggested by the results, appears to improve agreement between GDT and EIT.

In the next chapter, EIT and GDT are combined to measure properties of gas-liquid-solid flows in the bubble column in order to examine the effect of the solid phase on hydrodynamic behavior, particularly its effect on the distribution of the gas and liquid phases. These studies employ several different materials for the solid phase, all of which have conductive properties similar to air so that EIT can detect both the solid and gas phases. The density of each solid phase is significantly different from air, however, so that GDT can provide the information needed to determine the radial distributions of all three phases. The solid volume fraction in these three-phase tests is chosen to be well above 0.01, the uncertainty in EIT gas volume fractions based on the difference between GDT and EIT results in two-phase tests.

5. Investigation of Three-Phase Flows with EIT

With the electrical-impedance tomography system validated for quantitative measurements of two-phase flows, EIT and GDT were used in conjunction to make measurements of average and spatially resolved material distributions in a three-phase vertical bubble-column flow. This investigation served two purposes: (1) to further determine the usefulness of EIT in industrial multiphase flows, and (2) to investigate the effect of solids on slurry bubble-column reactor hydrodynamics and provide information which might be useful in the design and scaleup of such reactors (George *et al.*, 1999b).

For the two techniques to be used together, each phase in the gas-solid-liquid flow must have a unique combination of conductivity and attenuation properties. This study employed dry air as the gas phase and water with sodium nitrate as the liquid phase. For the solid phase, both polystyrene and glass were chosen. Polystyrene is an electrical insulator like air and has an attenuation coefficient similar to water, so that EIT is influenced by both the solid and gas phases but GDT is primarily sensitive to the gas alone. This marked difference in sensitivity of the two methods permits a first-order approximation, if desired, in reconstructions: the gas volume fraction profile from GDT may be subtracted from the insulating phase profile determined by EIT, yielding the solid and liquid phase distributions directly. Glass is also an insulator like air, but has an attenuation coefficient significantly different from both air and water, so that the first-order approximation does not hold in this case. Instead, the gamma attenuation formulas and the Maxwell-Hewitt relation must be solved as a set of simultaneous equations to reconstruct the radial volume fraction profiles of all three phases. This more accurate approach is used in all reconstructions presented in this chapter.

5.1. Experimental Setup

5.1.1. Testbed Setup

The three-phase experiments were conducted in the same Lexan bubble column used for the air-water tests described in Chapter 4. In each three-phase experiment, the column was initially filled with water and solids to a depth H_{col} of 144.8 cm, for a height-to-diameter ratio of $H_{col}/D_{col} = 7.6$. The 16 strip electrodes were centered on a plane $L = 82.0$ cm above the base ($L / D_{col} = 4.3$), again placing the region of EIT sensitivity completely under water. GDT scans were taken on two source-detector planes, located at $L = 70.6$ and 93.4 cm above the column base. These positions above and below the midplane of the EIT electrode ring were chosen to prevent obstruction by the electrodes, the cables exterior to the electrode ring, and the O-ring

Table 5.1. Properties of the materials used in the three-phase experiments.

material	ρ (g/cm^3)	μ (cm^{-1})	σ (μS/cm)	ω (μF/cm)
polystyrene	1.04	0.0866	$< 10^{-10}$	2.3×10^{-7}
glass	2.41	0.209	5.9×10^{-11}	$\approx 5\times10^{-7}$
water/$NaNO_3$	0.997	0.0856	242 – 432	$\approx 7\times10^{-6}$
air	0.00106	0.0000819	$\approx 10^{-10}$	8.86×10^{-8}

collars that joined the electrode ring to the remainder of the column. These locations also allowed verification that fully developed flow had been achieved at the measurement region.

The ring sparger used in the two-phase experiments (Figure 4.13) was again used to introduce dry air into the flow and to loft the solids from the column floor. To improve the lofting efficiency of the sparger for the denser glass spheres, the sparger was lowered (after the first experiments with polystyrene) to a position 6 cm above the base of the column. All tests were conducted at ambient pressure. The three cartridge heaters along the height of the column were again used to counteract evaporative cooling and maintain a constant temperature. The liquid temperature was held constant to within ±0.4ºC during experiments, which limited conductivity variations induced by temperature to ±0.6%.

5.1.2. Material Properties

The material properties of the phases used in these experiments are presented in Table 5.1. Deionized water was again used in the liquid phase, with controlled amounts of saturated sodium nitrate solution added to increase conductivity well above the lower limit of 200 μS/cm (Eq. 3.5) and provide a useful dynamic range of measured voltages. The initial DC conductivity of the aqueous sodium nitrate solution, measured before the first test at each solids loading, was $\sigma_L = 261\pm19$ μS/cm. As will be explained in Section 5.1.3, the conductivity consistently increased over the course of experiments as turbulence removed more coating material from the solids. The attenuation coefficient of glass in Table 5.1 was measured previously with the GDT system (Shollenberger *et al.*, 1997b), while the attenuation coefficients of polystyrene, air and water were obtained from the literature (Lamarsh, 1983; Thoraeus, 1965).

To determine whether the density and the size distribution of the solid particles can affect the behavior of the other phases, experiments were performed with a total of four different types of particles. The particles were chosen so that the effects of size and density could be observed separately. In the first series of three-phase tests, the polystyrene spheres described in the previous chapter (400 μm nominal diameter, 1.04 g/cm^3) were again used as the solid phase. Other particles used were polystyrene spheres of a smaller diameter (200 μm nominal) than the original polystyrene particles, and glass beads with smaller diameters (80 and 200 μm nominal) and a higher density (2.41 g/cm^3). The solid densities were measured by a volumetric method.

Photographs of each kind of particles used in this study and plots of their size distributions are shown in Figures 5.1 through 5.4. From Figure 5.4, it is apparent that some of

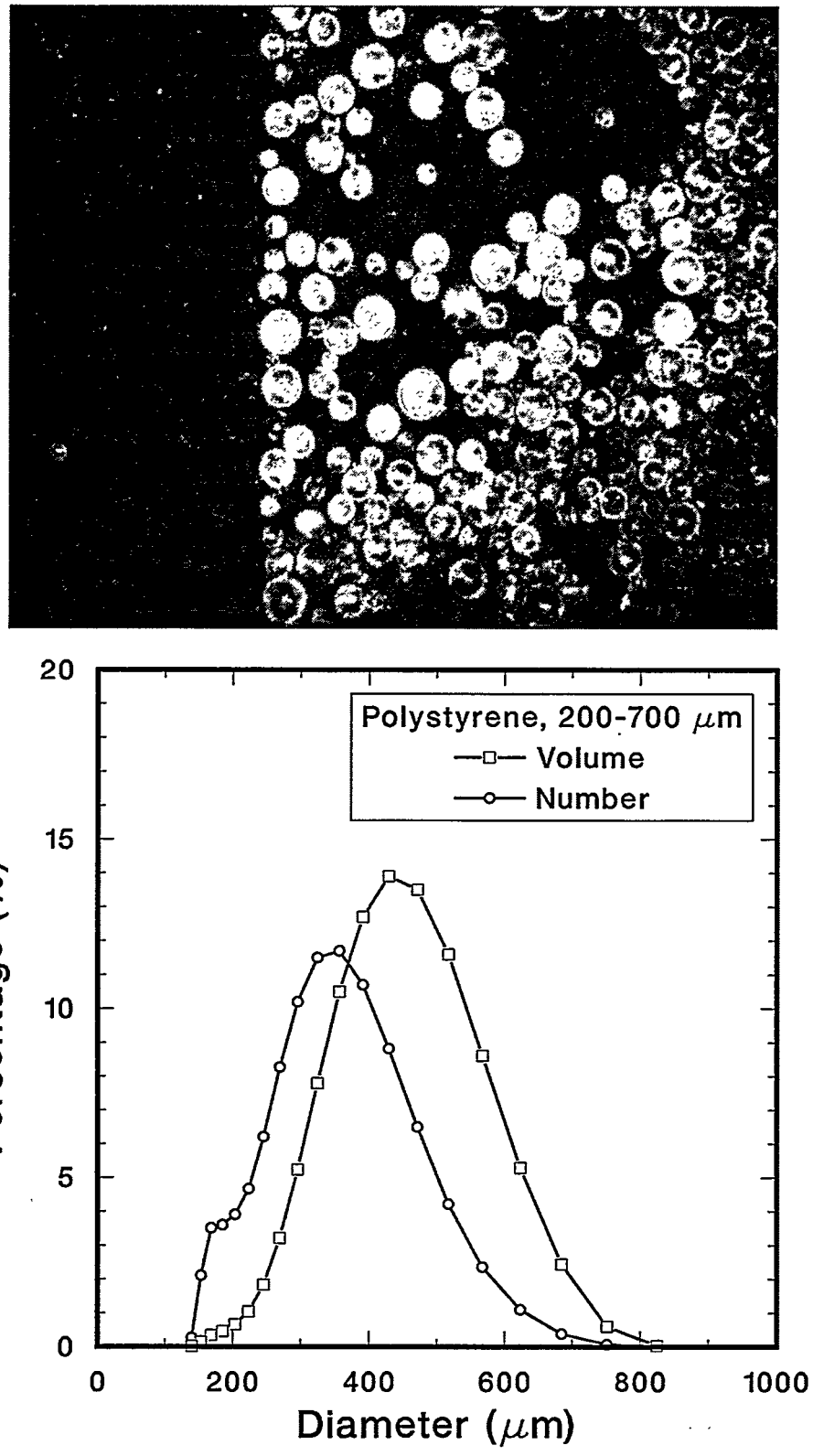

Figure 5.1. Photograph and size distribution of large polystyrene beads (diameter 200 – 700 μm, density 1.04 g/cm^3). The smallest ruler division in the photo is 500 μm.

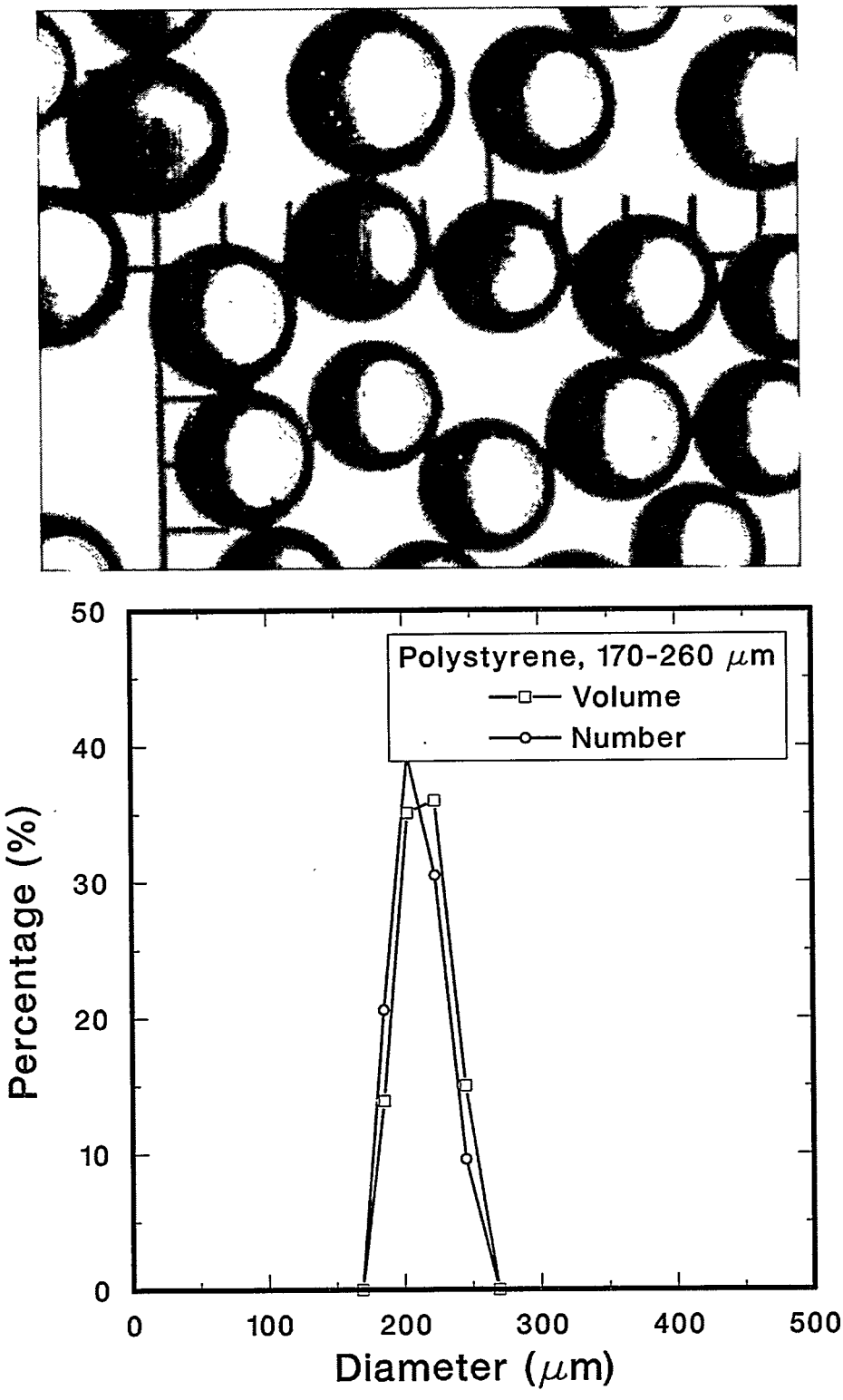

Figure 5.2. Photograph and size distribution of medium polystyrene beads (diameter 170 – 260 μm, density 1.04 g/cm^3). The smallest ruler division in the photo is 100 μm.

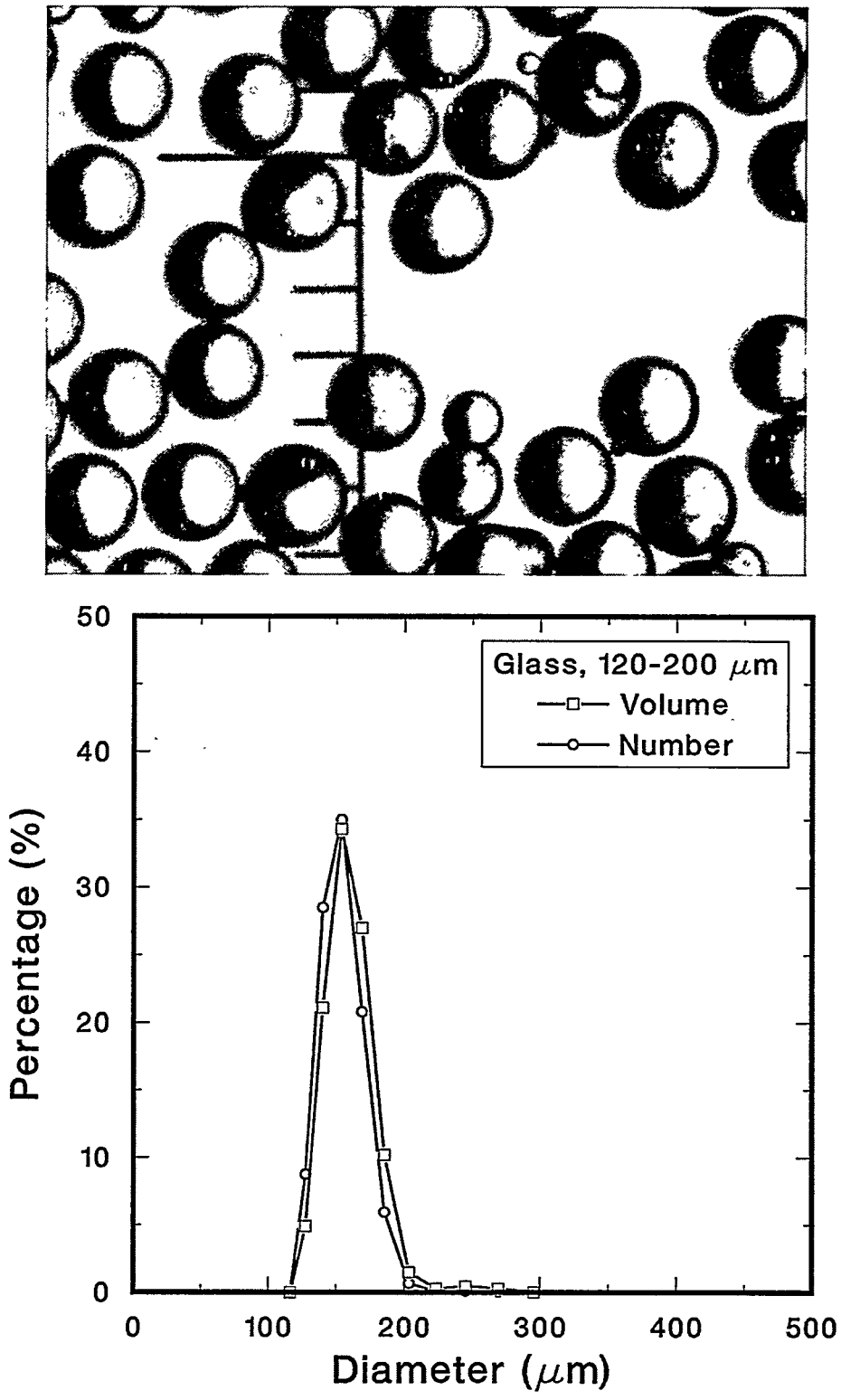

Figure 5.3. Photograph and size distribution of medium glass beads (diameter 120 – 200 μm, density 2.41 g/cm^3). The smallest ruler division is the photo is 100 μm.

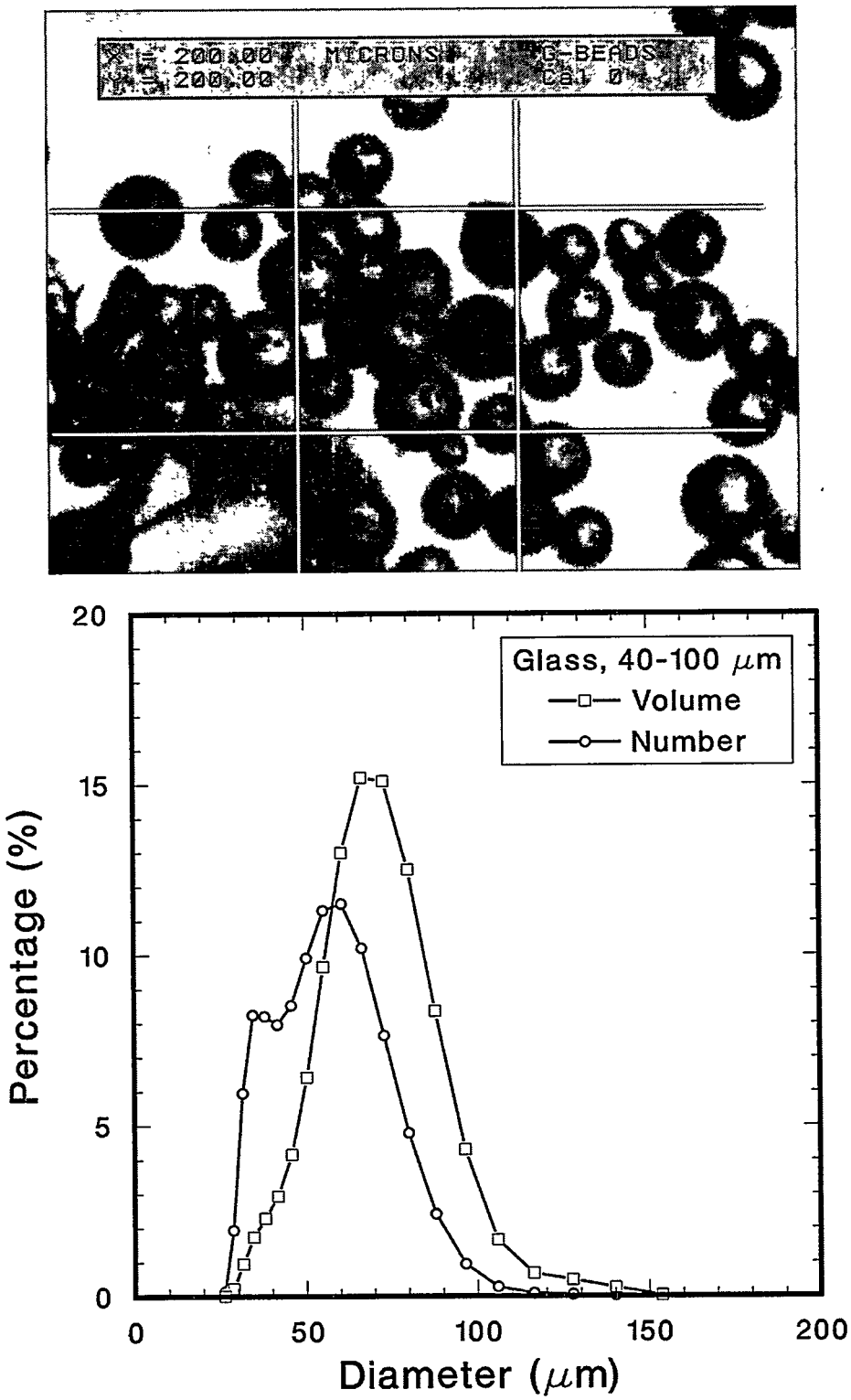

Figure 5.4. Photograph and size distribution of small glass beads (diameter 40 – 100 μm, density 2.41 g/cm^3). The central square in the photo is 200 μm on a side.

the "small" glass particles are decidedly aspherical; most are globular, but some elongated particles and shards are present. By comparison, the other particles are almost uniformly spherical. The graphs in each figure show the size distribution of each particle type, both in terms of number percentage and volume percentage, as determined by R. R. Lagasse using a Mie-scattering technique (Lagasse, 1999). The size distribution of the "large" polystyrene particles is seen to be broadest by far, with 98% of the volume of solids consisting of particles with diameters ranging from 200 to 700 μm. The "small" glass beads, the second type of particles to be investigated, are seen to have diameters generally in the range of 40–100 μm. The "medium" glass and polystyrene particles were both identified by their respective manufacturers as nominally 200 μm in diameter, but had notably different distributions: 120–200 μm for the glass spheres, 170–260 μm for the polystyrene.

5.1.3. Experimental Procedure

Before the first set of three-phase experiments, which involved polystyrene, the particles were washed and rinsed repeatedly to minimize the amount of soluble contamination carried with the solids into the liquid. Despite these efforts, noticeable amounts of opaque coating material were transferred from the polystyrene into the liquid by the turbulent flow. The opaque coating acted as a surfactant, as evidenced by foam at the top of the liquid column during gas flow. Electrolytes present in the coating material also altered the liquid conductivity over the course of experiments. To compensate for this effect of the contaminants, the standard procedure introduced in Chapter 4 of using the EIT system itself to measure the baseline liquid conductivity between tests was followed here as well.

The glass spheres also shed opaque material into the liquid during experiments. Although the glass particles were not washed before tests, the conductive effects of their contaminant were much less than that of the polystyrene, suggesting that a different coating was involved or perhaps that the "contaminant" was very small shards of broken particles. Again, baseline EIT conductivity measurements taken between flow conditions were used to compensate.

Table 5.2 lists the combinations of solid materials, solids loadings and gas volumetric flow rates at which measurements of phase distributions were made. Experiments were broken into subsets, each involving one nominal solid volume fraction $\bar{\varepsilon}_S^{NOM}$ defined as the ratio of the volume of solids to the combined reference volume of solids and liquid. Solid loadings up to $\bar{\varepsilon}_S^{NOM} = 0.30$ were included in the tests with large polystyrene particles; loadings for the other solids were limited to $\bar{\varepsilon}_S^{NOM} = 0.15$, the highest loading of glass particles that could be completely lofted at these gas flow rates. To obtain the desired solids loading for each subset, the total mass of required particles was computed from the reference volume (41.26 L, based upon a depth of $H_{col} = 144.8$ cm) and the known density of the solid material. Any amount of solids already present in the column from previous experiments was subtracted from this total to find the mass to be added. This mass was weighed out, introduced into the column, and allowed to settle to the bottom. After settling of the solids, liquid was drained from the column to return

Table 5.2. Three-phase experimental conditions analyzed with the EIT/GDT system.

Particle type	$\bar{\varepsilon}_S^{NOM}$	Q_G (L/min) 50	100	150	200	300	400	500
80 μm glass	0			X	X	X	X	
	5	a	a	X	X	X	X	
	10	a	a	X	X	X	X	
	15	a	a	a	X	X	X	
200 μm glass	0					X	X	X
	5	a	a	a	a	X	X	X
	10	a	a	a	a	X	X	X
	15	a	a	a	a	X	X	X
200 μm polystyrene	0	X	X	X	X	X	X	
	5	X	X	X	X	X	X	
	10	X	X	X	X	X	X	
	15	f	X	X	X	X	X	
400 μm polystyrene	0	X	X	X	X			
	5	X	X	X	X			
	10	X	X	X	X			
	22	X	X	X	X			
	30	f	X	X	X			

X = condition successfully measured
a = air flow rate inadequate to loft all solids
f = head of foam from surfactant in particle coating expanded to top of column

the total solid-liquid volume to the reference value, and an EIT scan was performed to measure the baseline liquid conductivity.

For each solids loading, air was introduced through the ring sparger at the chosen volumetric flow rate, Q_G, and the cartridge heaters were turned on during the flow to compensate for evaporative cooling. Over the course of all experiments, Q_G ranged from 50 to 500 L/min, corresponding to superficial gas velocities, U_G, of 2.9 to 29.2 cm/s. The flows were all churn-turbulent and opaque, even at the lowest solids loading and lowest gas flow rate (see Figure 5.5). At higher gas flow rates, non-spherical voids were occasionally visible at the column walls.

In each successful test, the downward flow of air from the sparger was sufficient to loft all the solids from the bottom and produce a three-phase flow throughout the column. No measurements were made for certain combinations of gas flow rate and solid volume fraction, marked "a" in Table 5.2, because an appreciable amount of solid particles remained at the bottom of the column under these conditions. Although these particles could be lofted by temporarily increasing the air flow rate, they settled to the bottom of the column when the air flow rate was returned to the prescribed value. It should be noted that cases of "0%" nominal

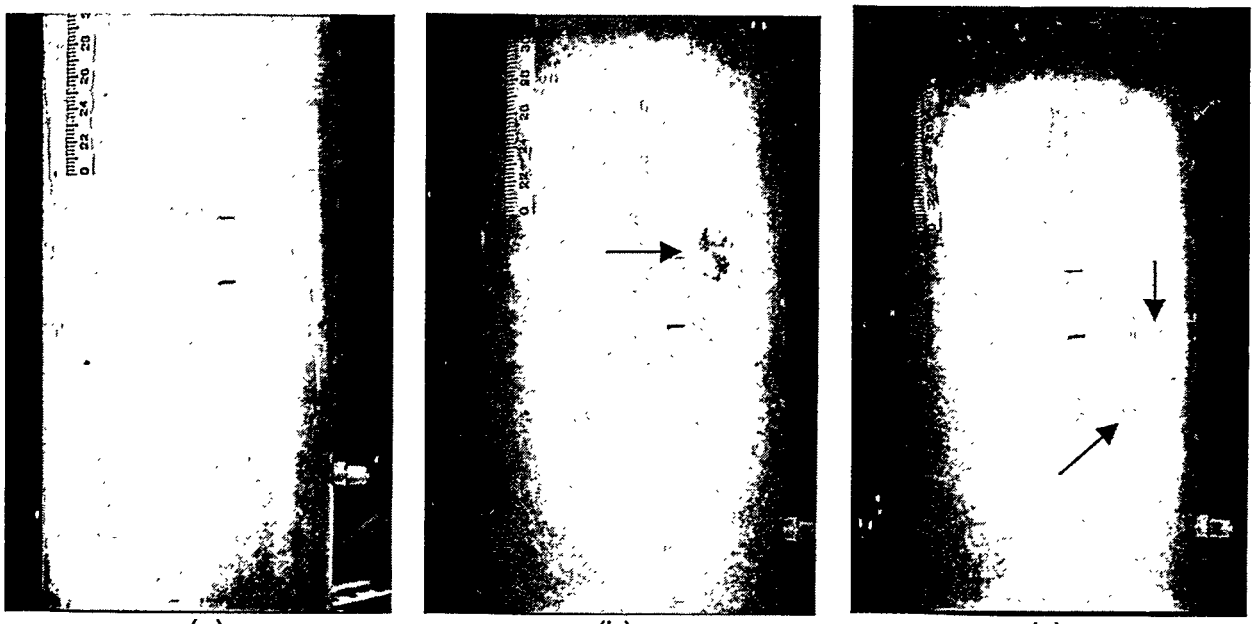

Figure 5.5. Photographs of flow conditions in three-phase, polystyrene-air-water flows in the transparent bubble column. (a) $\bar{\varepsilon}_S^{NOM}$ = 0.05, Q_G = 50 L/min; (b) $\bar{\varepsilon}_S^{NOM}$ = 0.10, Q_G = 200 L/min; (c) $\bar{\varepsilon}_S^{NOM}$ = 0.22, Q_G = 100 L/min. Note the air voids at the walls (marked by arrows) at the higher gas flow rates, indicating a churn-turbulent gas flow regime. The solid phase is 400 μm polystyrene particles; the vertical scale is in centimeters.

solid volume fraction employ water in which solids previously added were removed for the test, leaving coating material in the water. This was necessary to ensure that the surface tension was the same for all experiments, both with and without solids present. Table 5.2 also notes flow conditions which were attempted but not completed because the surfactant foam above the solid-liquid slurry expanded and threatened to overflow the top of the column.

As shown in Table 5.1 and discussed in the introduction to this chapter, the polystyrene and water attenuation coefficients for ^{137}Cs gamma rays are nearly the same. Since gamma attenuation and density are roughly proportional for the lighter elements, it is not unexpected that polystyrene is nearly neutrally buoyant in water, and that it is easily lofted and mixed with the other phases by the downward air jets from the sparger. Glass, however, has both a density and gamma attenuation coefficient significantly higher than those of water. Because of the higher density, some air flow rates that easily lofted an entire polystyrene loading were inadequate to loft the same volume of negatively buoyant glass. As a result, minimum and maximum flow rates for three-phase tests involving glass were higher than those in polystyrene tests. Lofting efficiency was also influenced to some extent by particle diameter; tests with 200 μm glass spheres required higher minimum flow rates than tests with 80 μm glass spheres.

Profile measurements at each flow condition consisted of a GDT scan at the lower scan plane, followed by an EIT scan, followed by a second GDT scan at the upper plane. After the profile measurements were completed at each condition, gas flow was terminated, and the solids

were allowed to settle beyond the EIT measurement region to the bottom of the column. This settling process required 15 to 60 minutes, depending upon the amount and type of solids present. Following the settling period, EIT was applied again to measure changes in the baseline conductivity of the liquid. The values of liquid conductivity measured before and after each set of flow conditions were averaged and used to compute volume fraction profiles under those conditions. In the experiments involving polystyrene, a fraction of the particles floated to the free surface of the liquid during the post-test settling period. This layer of solids was not disturbed during the settling period or the EIT baseline measurements, but was forced back into the liquid before the next test by a single Taylor bubble created from a momentary air flow.

For each flow condition, the information from the pair of GDT scans was averaged and combined with the EIT data to determine the radial volume fraction profiles at the EIT electrode plane. As shown in the results later in this chapter, the two GDT scans did not differ from each other by more than 0.01 in ε_G for all cases tested. For the first experiments with 400-μm polystyrene particles, the original 486 PC was used to operate the EIT package. Twenty-five EIT projection sets were acquired in fast mode during each flow condition over a period of about 20 seconds and averaged to yield voltage data for reconstructions. This averaging was required in order to combine the EIT results with the average of the two GDT scans. After the first polystyrene experiments, several changes were made to the EIT system, including the replacement of the 486 with a Pentium PC and the addition of the quartic reconstruction algorithm. Uncertainty analyses of the quartic algorithm (described in Section 3.3.4) mandated that a total of 100 projection sets be collected and averaged for the remaining tests, while difficulties with memory management on the Pentium restricted data acquisition to slow mode. As a result, EIT reconstructions for the remaining three-phase tests represented averages over a period of 2 ½ minutes, instead of the twenty-second period originally required. By comparison, the GDT scans involved data acquisitions over 60 seconds along each of 19 beam paths, so that their reconstructions were averages over a period of 23 minutes. However, since the measurements of two-phase flows in Chapter 4 demonstrated that any differences in temporal averaging by GDT and EIT do not significantly affect results, it is believed that combining these data averaged over different periods to determine the three-phase distributions does not introduce unwarranted error.

5.2. Calculation of Phase Volume Fraction Profiles

The data from the GDT and EIT scans may be combined for three-phase flows by modifying the basic equations used with each method to account for the presence of all three phases. In the case of a purely two-phase, gas-liquid flow, the two-phase continuity equation and the Maxwell-Hewitt relation are used with conductivity distributions from the EIT reconstruction code to determine liquid and gas volume fraction profiles. In the more general three-phase case, the quantity $(1-\varepsilon_L)$ in Eq. 3.13 is equivalent to the total insulating phase fraction ε_I, which includes both the solid and gas phases in this study. The three-phase continuity equation is therefore

$$\varepsilon_S + \varepsilon_L + \varepsilon_G = \varepsilon_I + \varepsilon_L = 1. \tag{5.1}$$

The solid and gas volume fractions must be separated from ε_I using GDT attenuation information.

This section presents the relations used in this study to determine the radial variations of ε_G, ε_L and ε_S from the radial variations of the normalized gamma attenuation f_μ and the normalized electrical conductivity $\sigma(r)/\sigma_L$. Each term in Eq. 5.1 is implicitly a function of position in the flow. In this investigation only radial variations in the phase distributions are considered, since the reconstruction codes `EITAXI` and `GDTAXI` assume invariance in θ and z in the conductivity and attenuation distributions. The derivations will therefore explicitly show dependencies only upon r.

In either the two-phase or three-phase case, the liquid profile may be determined directly from the reconstructed conductivity profile by solving the Maxwell-Hewitt relation for ε_L. In the original three-dimensional formulation, for example, Eq. 3.13 becomes

$$\varepsilon_L(r) = \frac{3\sigma(r)}{2\sigma_L + \sigma(r)}. \tag{5.2}$$

The GDT reconstruction algorithm, initially developed for use with gas-liquid flows, produces a normalized radial attenuation distribution of the form

$$f_\mu(r) = \frac{\mu(r) - \mu_G}{\mu_L - \mu_G}. \tag{5.3}$$

The measured local value of $\mu(r)$ is a weighted average of the attenuation of all phases over a differential volume at r, so that in the three-phase case,

$$\mu(r) = \mu_S\varepsilon_S(r) + \mu_L\varepsilon_L(r) + \mu_G\varepsilon_G(r). \tag{5.4}$$

Combining Eqs. 5.1 through 5.4 allows the distributions of all three phases in the flow to be solved for. The only pieces of information required to compute $\varepsilon_L(r)$, $\varepsilon_G(r)$ and $\varepsilon_S(r)$ are $f_\mu(r)$, determined from GDT data; $\sigma(r)$, determined from EIT data; and four physical properties known *a priori*: the phase attenuation coefficients μ_S, μ_L, and μ_G and the liquid conductivity σ_L.

While the approach of Eqs. 5.1 through 5.4 is a general one, the equation for $\varepsilon_L(r)$ is subject to change, specifically with the assumptions inherent in the Maxwell-Hewitt relation. Recall that the relation was successfully modified in Chapter 4 (see Eq. 4.4) to improve agreement between GDT and EIT in gas-liquid flows, based on the assumption of slight vertical motion of the bubbles during EIT measurements. The Maxwell-Hewitt relation was also shown in Chapter 3 to be acceptably accurate for volume fractions of bimodal bubble sizes, although insulators of a single size are assumed in its derivation. With these facts in mind, empirical

adjustments were made to the original Maxwell-Hewitt relation with the intent of extending its applicability to the three-phase flows of this chapter and improving reconstruction accuracy.

The changes involve two assumptions related to these three-phase flows. First, the solid and the gas are treated by EIT as a single insulating phase. Second, a general Maxwell-Hewitt relation is assumed that involves a coefficient, α, dependent upon the domain geometry: $\alpha = 1$ for two-dimensional cylindrical inclusions or $\alpha = ½$ for three-dimensional spherical bubbles. Under these assumptions, Eqs. 3.13 and 3.14 may be generalized to the following equation for normalized conductivity:

$$\sigma/\sigma_L = E[\varepsilon_G + \varepsilon_S, \alpha]. \tag{5.5}$$

Here, σ, ε_G and ε_S are implicitly functions of r. The form of the function E is defined by the Maxwell-Hewitt relation as

$$E(\xi,\alpha) = \frac{1-\xi}{1+\alpha\xi}. \tag{5.6}$$

Note also that

$$E[E(\xi,\alpha),\alpha] = \xi. \tag{5.7}$$

As discussed in Section 3.3.3 and George *et al.* (1999b), the first assumption can be modified to represent the bimodal distribution of "particle" sizes (*i.e.*, bubbles and solid particles) by treating the three-phase flow as gas bubbles within a liquid-solid mixture. In this case the modified Maxwell-Hewitt relation is applied recursively, first to the solid particles in the liquid phase, then to the gas in the liquid-solid mixture. As suggested in Chapter 4, it may also be appropriate to empirically modify the value of α from ½ to ⅗ for time-averaged three-dimensional reconstructions. The following relation then replaces Equation 5.5:

$$\sigma/\sigma_L = E(\varepsilon_G, \tfrac{3}{5})E[\varepsilon_S/(\varepsilon_S + \varepsilon_L), \tfrac{3}{5}]. \tag{5.8}$$

This modified relation is used in all three-phase analyses in the remainder of this chapter.

The approach outlined in this section is incorporated into the reconstruction code `GDTEIT`, listed in Appendix J. In the reconstructions, the conductivity distributions determined by `EITAXI` and input to `GDTEIT` were modeled as a quartic function in r, symmetric about the column axis. Similarly, chord-averaged attenuation coefficients computed from GDT data were fit to a fourth-order polynomial by `GDTAXI` before the Abel transform was taken so that the distribution data input to `GDTEIT` from both methods were of the same order.

5.3. Results and Discussion

5.3.1. Three-Phase Results and Observed Trends

The complete set of phase volume fraction profiles for all solids loadings and gas flow rates may be found in Appendix K. Relevant graphs from the appendix are repeated in Figures 5.6 and 5.7 to illustrate points of discussion later in this section. Several general observations can be made about the results. First, as expected, the gas volume fraction increases as the superficial gas velocity is increased. The gas volume fraction profiles behave like those found in gas-liquid flows, increasing with U_G preferentially on the column axis. Generally, the profiles $\varepsilon_S(r)$ and $\varepsilon_L(r)$ of the other phases decrease with rising U_G, as the volume of gas in the column increases and the constant amounts of solid and liquid occupy a smaller fraction of the total volume. Second, the combined reconstruction algorithm produces a small but nonzero solid-volume-fraction profile even when no solid particles have been added to the column. Based on the individual uncertainties of the separate EIT and GDT methods, an uncertainty around ±0.02 for volume-fraction profiles has been assigned to the combined algorithm. The fact that the computed solids profiles are generally less than 0.01 when no solids are present is in harmony with this combined uncertainty. Third, the solid-volume-fraction profiles have a variety of shapes, including concave upward, a central maximum, and a maximum at a radial location between the axis and the wall. In most cases, these variations lie within or close to the indicated uncertainty and should not be considered significant. Possible exceptions are the profiles of 400 μm polystyrene particles at volume fractions of 0.22 and 0.30; these profiles were calculated from 25 EIT projection sets rather than 100, and so are expected to have higher uncertainties.

A significant observation is demonstrated in Figure 5.6, which shows the gas volume fraction profiles for a superficial gas velocity of 8.8 cm/s and four different solid volume fractions of 400 μm polystyrene particles. The gas profile is identical in all four plots to well within the ±0.02 accuracy limit, suggesting that replacement of up to 30 volume percent of the liquid with solids of similar density has little or no effect on the gas distribution. Figure 5.7 shows similar radial volume-fraction profiles for the 200 μm glass beads. The addition of glass particles consistently reduces the gas volume fraction by a small amount, but for solid volume fractions as high as 15%, the decrease is comparable to the experimental uncertainty. Indeed, for all of the particle types and gas flow rates examined, the gas volume fraction radial profiles were unaffected by the addition of solids to within an uncertainty band equal to the experimental uncertainty of ±0.02 in volume fraction.

Domain-averaged phase volume fractions were also computed from the reconstructions. The effect of the presence of solids on average gas volume fraction is quantified in Figures 5.8 through 5.11, which show plots of $\bar{\varepsilon}_G$ for all four particle types. In all cases $\bar{\varepsilon}_G$ is seen to increase monotonically with U_G, as expected. Decreases in average gas volume fraction with increasing solids density (glass versus polystyrene) are strongly suggested by the plots. The

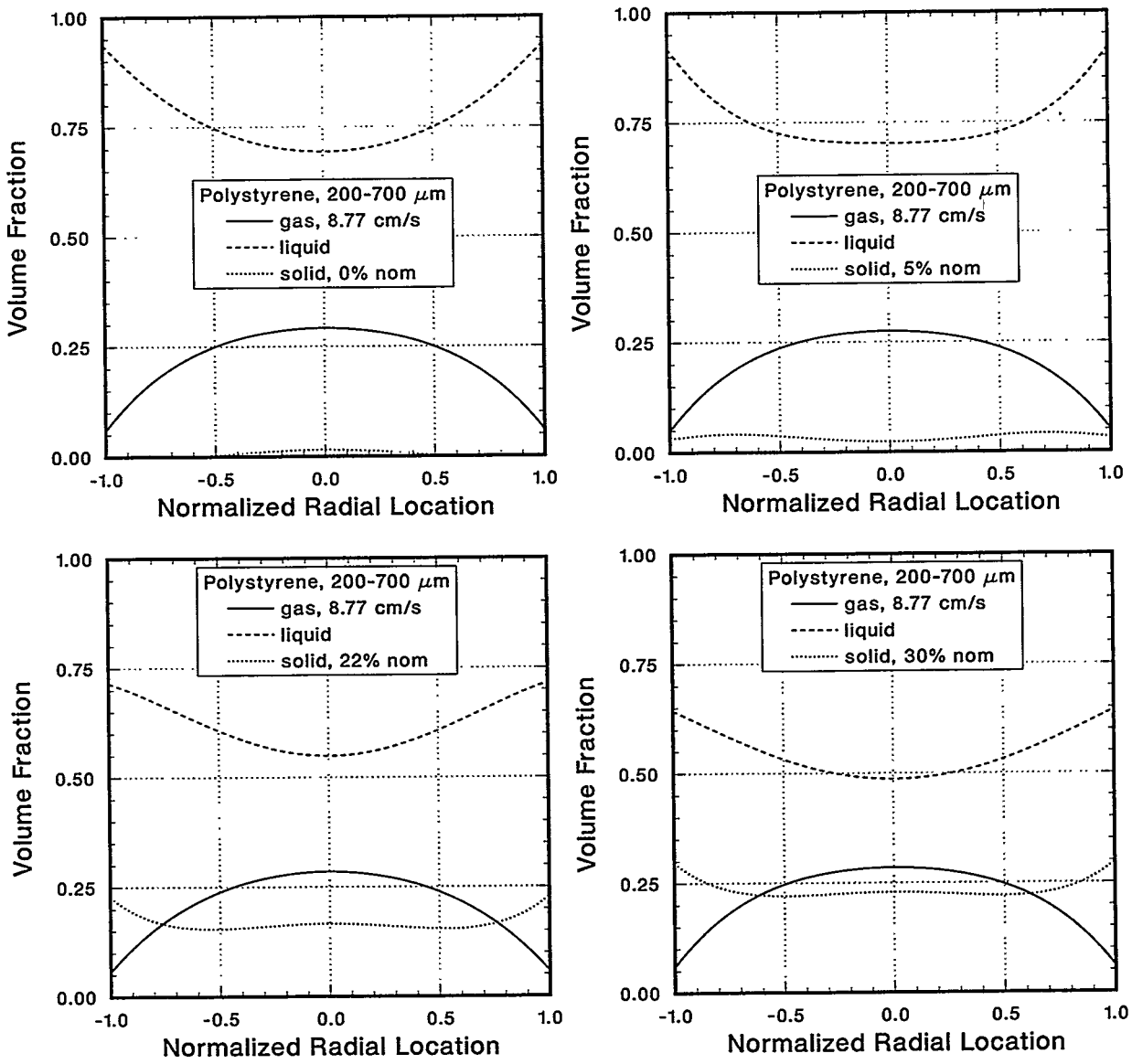

Figure 5.6. Phase volume fraction profiles determined from EIT and GDT reconstructions for a superficial gas velocity of U_G = 8.8 cm/s and a solid phase of 400 μm polystyrene particles. Nominal solid volume fractions $\bar{\varepsilon}_S^{NOM}$ are listed in each plot.

graphs involving glass particles also show a clear decrease in gas volume fraction (by as much as 0.04 in $\bar{\varepsilon}_G$) with increasing solid volume fraction, but no such trend is observed for the polystyrene spheres. As with Table 5.2, a nominal solid volume fraction of 0% in these graphs indicates cases in which particles loaded for previous experiments have been removed from the water, leaving coating material behind.

Figure 5.12 is a compilation of average gas volume fractions for all two-phase and three-phase experiments performed in the Lexan bubble column to date and presented separately in Figures 5.8 through 5.11. For comparison, Figure 5.12 also shows the average gas volume fractions obtained using clean, deionized water and no solids. These "clean" volume fractions

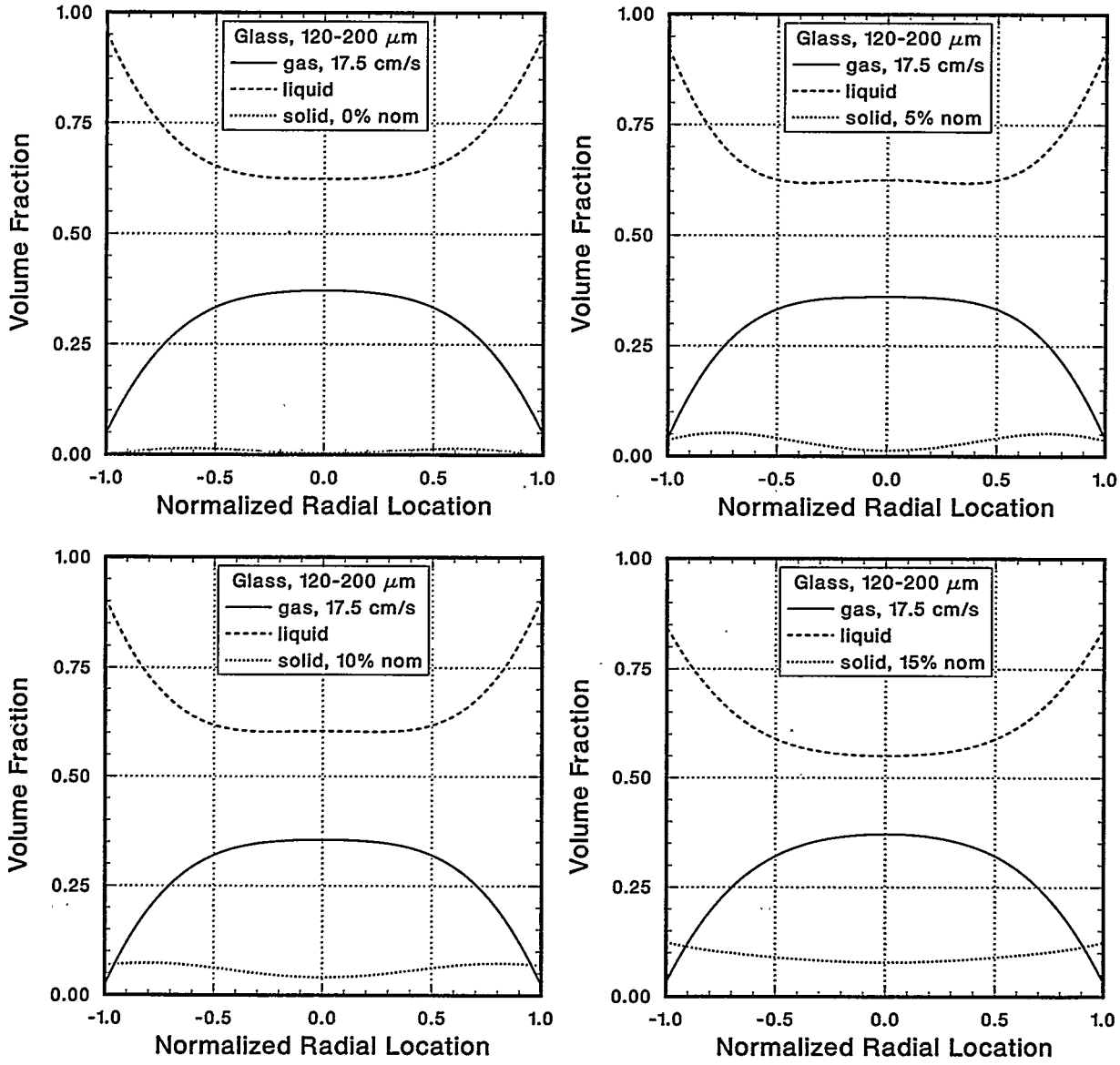

Figure 5.7. Phase volume fraction profiles determined from EIT and GDT reconstructions for a superficial gas velocity of U_G = 17.5 cm/s and a solid phase of 200-μm glass particles. Nominal solid volume fractions $\bar{\varepsilon}_S^{NOM}$ are listed in each plot.

are considerably lower than for the cases in which particles are employed, but all results can be described to within ±0.04 by a curve passing through the middle of the data. As noted earlier, the addition of particles also unavoidably adds surfactants, which reduce surface tension and change the gas volume fraction $\bar{\varepsilon}_G$ by +0.02 to +0.06, substantially more than the change produced by the particles themselves. This indicates that caution should be exercised in determining "three-phase" effects, which may result from spurious surface-tension changes instead of the presence of particles.

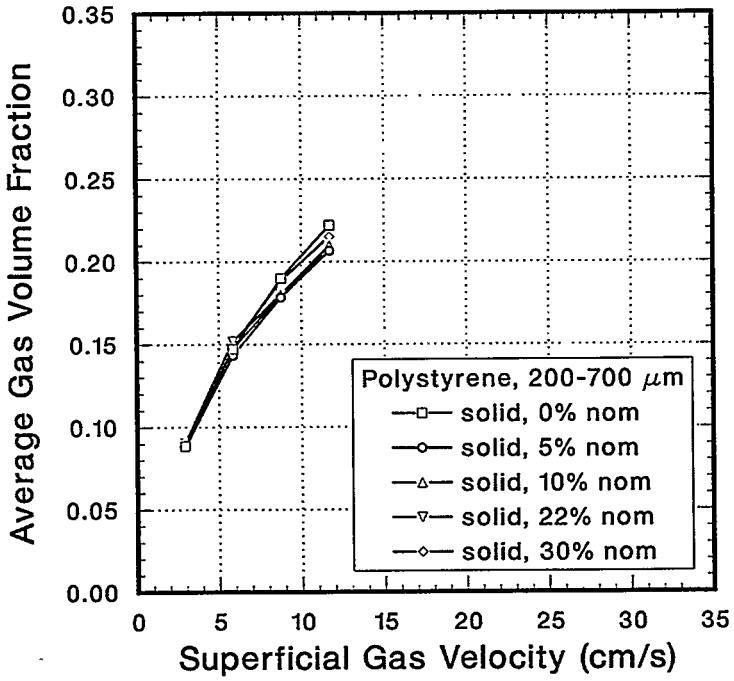

Figure 5.8. Average gas volume fractions for large (400 μm nominal diameter) polystyrene beads.

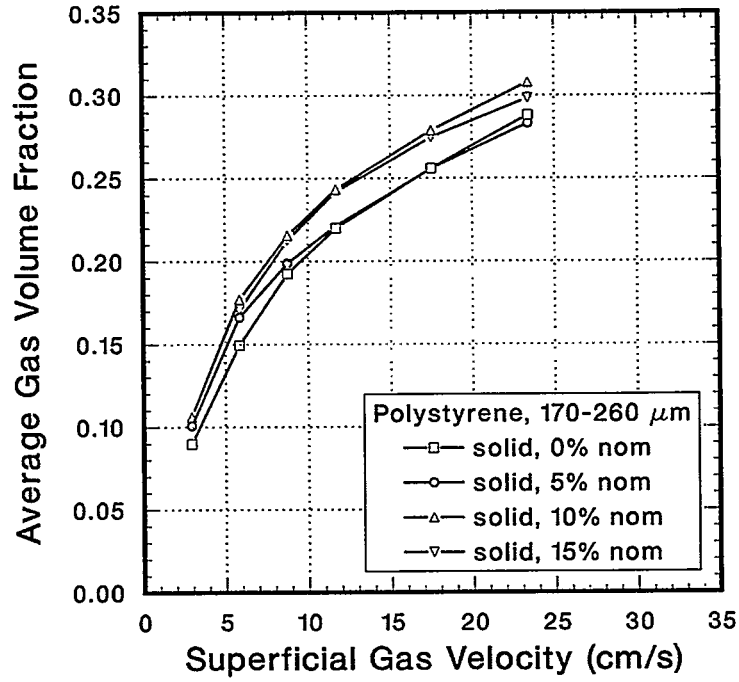

Figure 5.9. Average gas volume fractions for medium (200 μm nominal diameter) polystyrene beads.

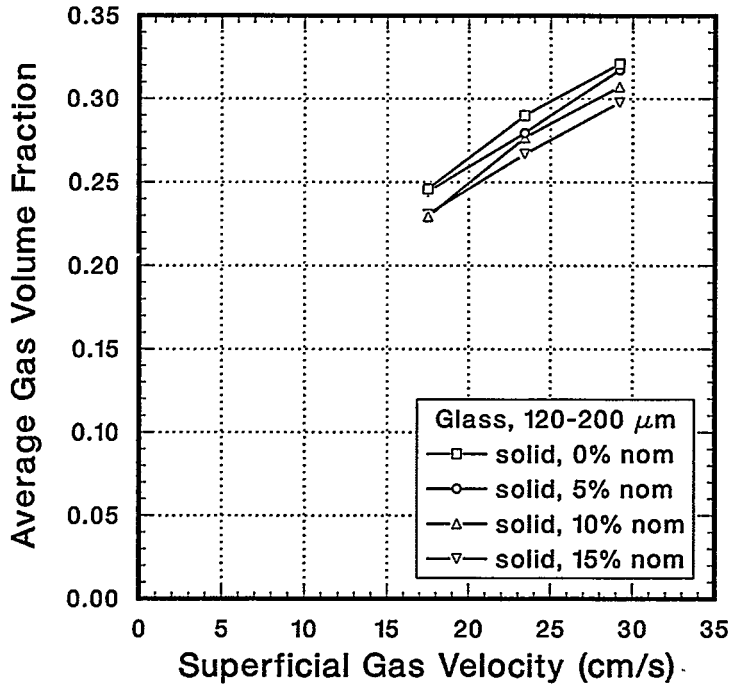

Figure 5.10. Average gas volume fractions for medium (200 μm nominal diameter) glass beads.

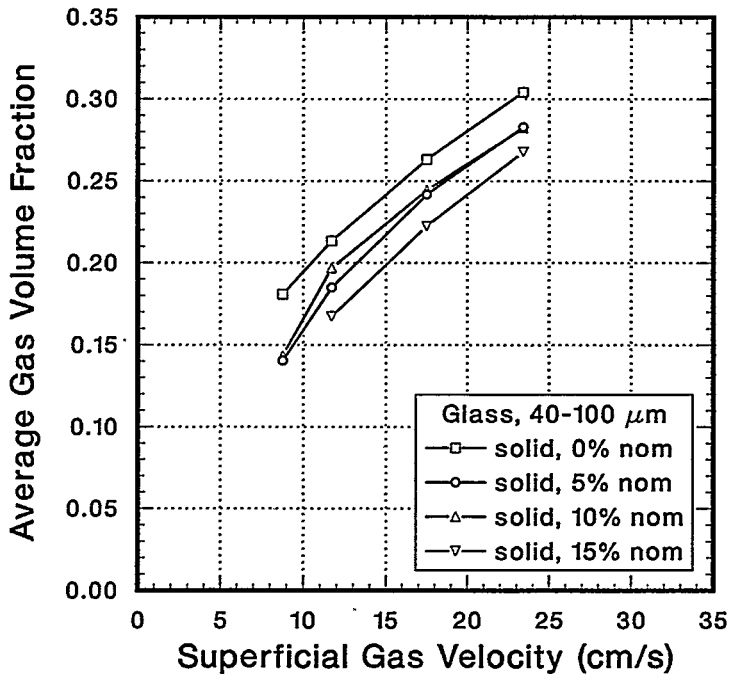

Figure 5.11. Average gas volume fractions for small (80 μm nominal diameter) glass beads.

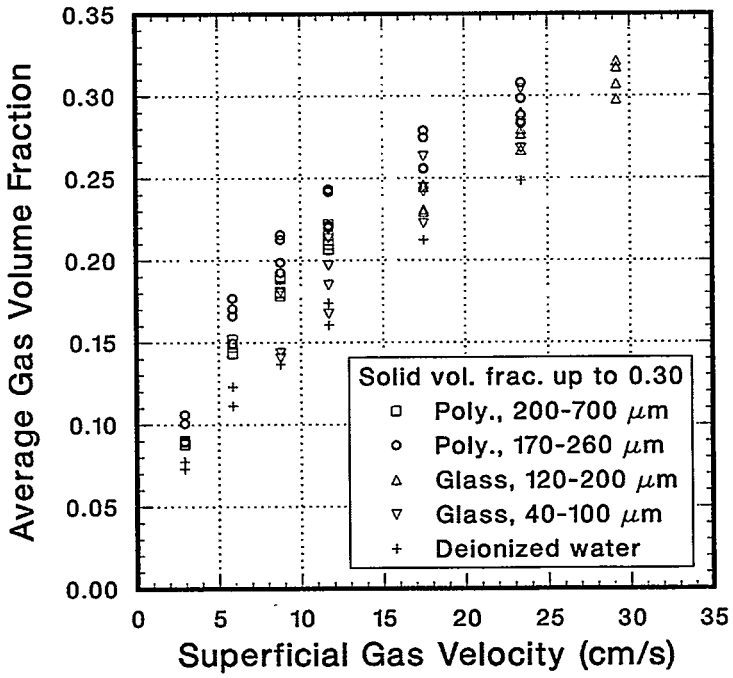

Figure 5.12. Average gas volume fractions for all two-phase and three-phase experiments to date.

As observed earlier, solid phase density appears to influence gas distributions. For glass particles, particularly the 80 μm particles, the gas-volume-fraction profiles decrease slightly in magnitude as the solids loading is increased. This is quantified in Figure 5.13, where the average gas volume fraction is plotted against the nominal solid volume fraction of glass particles for all values of the superficial gas velocity. Despite the uncertainty around ±0.02 in the average values, $\bar{\varepsilon}_G$ clearly decreases with increasing nominal solid volume fraction of glass. The corresponding graph for the less dense polystyrene spheres, Figure 5.14, shows that changes in the gas volume fraction with solid volume fraction are smaller and fall within the experimental uncertainty about the data. While the gas volume fraction appears to increase for $\bar{\varepsilon}_S^{NOM} \leq 0.1$ of the medium polystyrene, $\bar{\varepsilon}_G$ decreases as the solid fraction increases further, and remains within the ±0.02 uncertainty band. Direct comparison of the gas volume fractions for the cases of 200 μm polystyrene and 200 μm glass (at Q_G = 300 and 400 L/min) shows that for $\bar{\varepsilon}_S^{NOM} \geq 0.1$, $\bar{\varepsilon}_G$ differs by 0.035 to 0.04, twice the measurement uncertainty. Though not conclusive, these observed effects of solids density and loading are in good agreement with an effective two-phase model for these flows discussed in the next section.

A small diameter effect is noted in that values of $\bar{\varepsilon}_G$ are consistently slightly higher for the "medium" (200 μm) polystyrene spheres than for the "large" (400 μm) polystyrene spheres, but again, the differences are comparable to the uncertainty of ±0.02. No significant diameter effect is observable between the "small" and "medium" glass particles, however. Overall, the maximum change in average gas volume fraction with both particle density and size is ±0.04, which is less important than changes from contaminants and the resulting surface-tension changes evidenced in Figure 5.12.

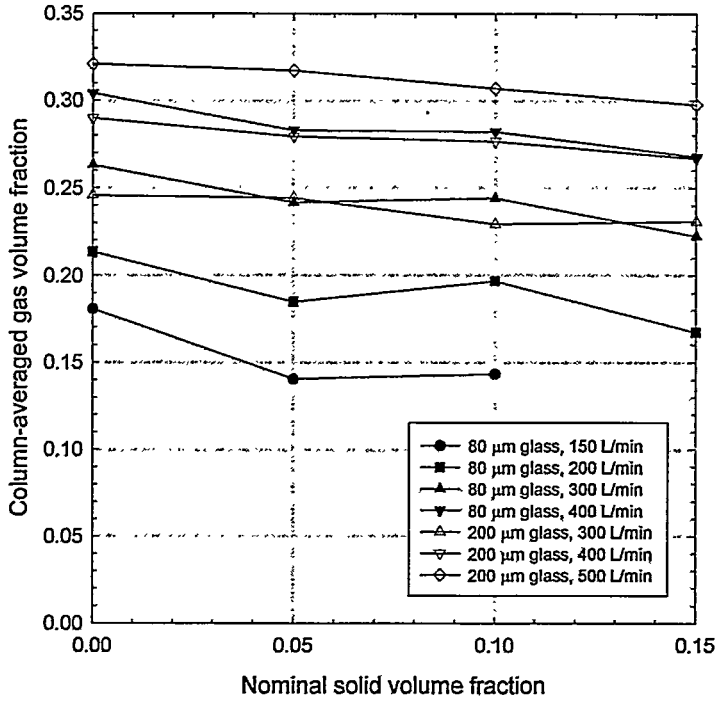

Figure 5.13. Dependence of average gas volume fraction on nominal solid volume fraction for all three-phase experiments involving glass particles.

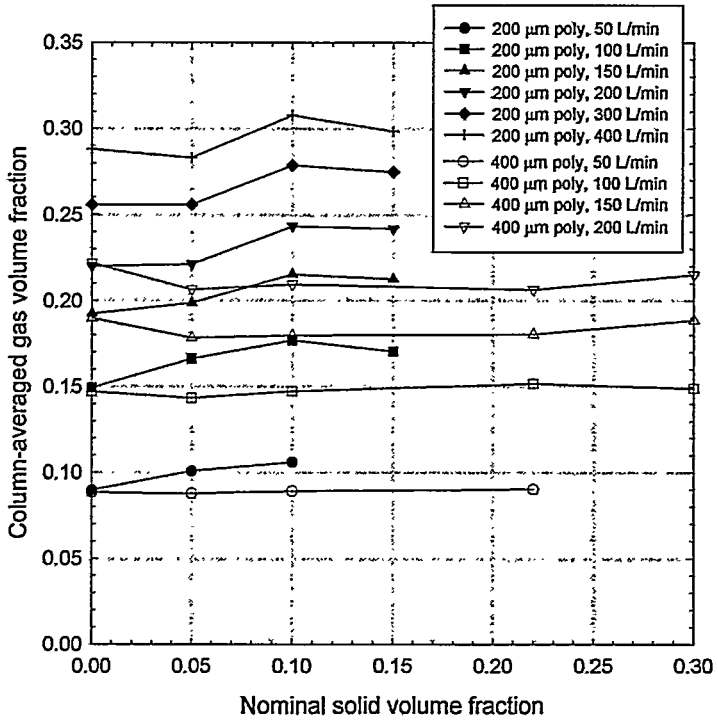

Figure 5.14. Dependence of average gas volume fraction on nominal solid volume fraction for all three-phase experiments involving polystyrene particles.

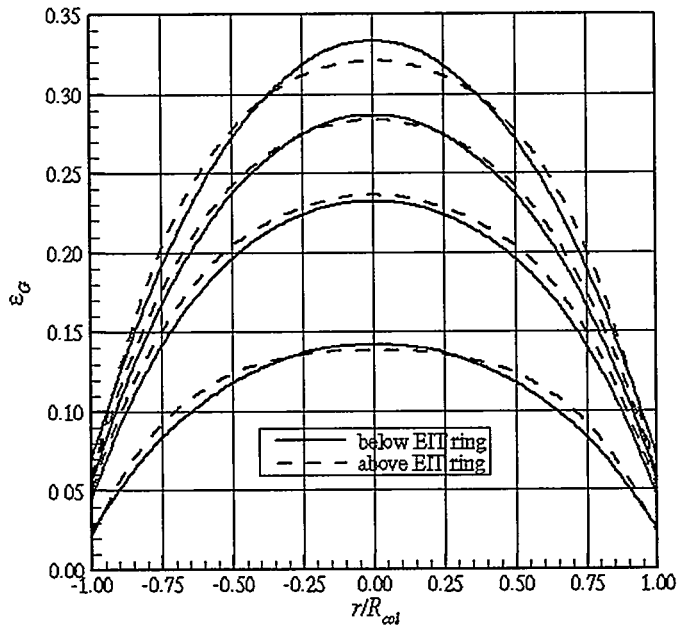

Figure 5.15. Comparison of gas profiles computed from GDT attenuation data taken above and below the EIT electrode ring for $\bar{\varepsilon}_S^{NOM} = 0.22$. From bottom to top, the curve pairs correspond to superficial gas velocities U_G of 2.9, 5.9, 8.8, and 11.7 cm/s.

5.3.2. Error Analysis and Model Refinement

A brief analysis was performed to quantify the potential error due to vertical averaging. For each flow condition, a single liquid-phase profile was determined from the EIT projection sets, whereas two attenuation profiles were determined with GDT — one above the electrode ring, the other below. The average of the two attenuation profiles was combined with the liquid profile to obtain phase volume fraction profiles at the electrode plane. Figure 5.15 presents preliminary gas profiles computed separately from each attenuation profile for the case of 400 μm polystyrene spheres, $\bar{\varepsilon}_S^{NOM} = 0.22$ and all gas flow rates. The gas profile pairs are identical to within 0.01, the accuracy of EIT determined during validation tests. This agreement suggests that at this solids loading, the flow was approximately fully developed by the time it reached the measurement region. Comparisons were also made for other randomly chosen polystyrene loadings. For $\bar{\varepsilon}_S^{NOM} < 0.22$, the difference in profiles is smaller, while for $\bar{\varepsilon}_S^{NOM} = 0.30$, the difference approaches 0.04 in ε_G. This variation with vertical location may indicate that the flow was still developing at the measurement region, although inadequacies in the original Maxwell-Hewitt relation discussed below are more likely explanations for the difference.

An improvement to the constitutive model was made after comparison of the data to a simple phase distribution model. Because of the similarity in two-phase and three-phase

experimental results, it is appealing to attempt to interpret gas-liquid-solid experiments in terms of gas-liquid experiments in which the "liquid" (more properly, the "dense phase") is taken to have effective properties corresponding to the actual liquid-solid mixture. Such models often assume that the solid phase is dispersed homogeneously and entirely within the liquid phase, so that the spatial distributions of the two dense phases are proportional to one another for all gas flow rates at a constant solids loading. The uncertainty in the reconstructions makes it difficult to test the assumption of homogeneity by directly comparing solid and liquid profiles. Instead, the ratio of the domain-averaged solid volume fraction $\bar{\varepsilon}_S$ to the domain-averaged dense phase volume fraction $(\bar{\varepsilon}_S + \bar{\varepsilon}_L)$ was computed for representative test conditions. If the above assumption about solid and liquid distribution were true, the ratio $\bar{\varepsilon}_S /(\bar{\varepsilon}_S + \bar{\varepsilon}_L)$ would equal $\bar{\varepsilon}_S^{NOM}$ at all gas flow rates, even in the presence of significant axial and radial variations in the phase distributions.

Figure 5.16 presents the ratio $\bar{\varepsilon}_S /(\bar{\varepsilon}_S + \bar{\varepsilon}_L)$ as a function of superficial gas velocity and nominal column-averaged solids loading $\bar{\varepsilon}_S^{NOM}$ (denoted by the dashed lines) for the 400 μm polystyrene particles, the first solids used. These values were computed from the known masses of solid and liquid phases in the column. The curves were produced using the original Maxwell-Hewitt relation (Eq. 3.13), before the recursive relation or the modified coefficient of $\alpha = 3/5$ were developed. At all solids loadings, the ratio appears to increase above the nominal value as the superficial gas velocity U_G increases, which is counter-intuitive. Two possible causes for this trend were identified. The first was EIT measurement inaccuracies resulting from the increasing fraction of insulating phases (solid and gas) in the flow, which approached $\varepsilon_I = 0.50$ at the highest solids loading and gas flow rate. The second explanation was the inadequacies in the original Maxwell-Hewitt relation that led to the derivation of the modified relation.

Figure 5.17 shows the results when the original Maxwell-Hewitt relation is replaced with the recursive, bimodal Maxwell-Hewitt relation (Eq. 5.8). The values of $\bar{\varepsilon}_S /(\bar{\varepsilon}_S + \bar{\varepsilon}_L)$ now generally lie below the values of $\bar{\varepsilon}_S^{NOM}$, the ideal values if the solid were distributed uniformly throughout the liquid, and approach these nominal values as the superficial gas velocity is increased. Since larger superficial gas velocities agitate the medium more severely, it would not be surprising to find that the solid-liquid mixture became more uniform at larger superficial gas velocities. In the interest of expediency, average values were used instead of profiles to produce this plot, so it is suggested that this analysis be repeated in the future using the profiles themselves to verify these observations. Nevertheless, these results suggest that the modified Maxwell-Hewitt relation has improved further the accuracy of material-distribution profile measurements, and that the high insulating volume fractions did not pose problems for EIT in these experiments.

5.3.3. Correlation of Data

Typically, experimental results are correlated using three liquid properties: density, viscosity and surface tension. Recall from Section 2.2.1 that greater liquid density increases the

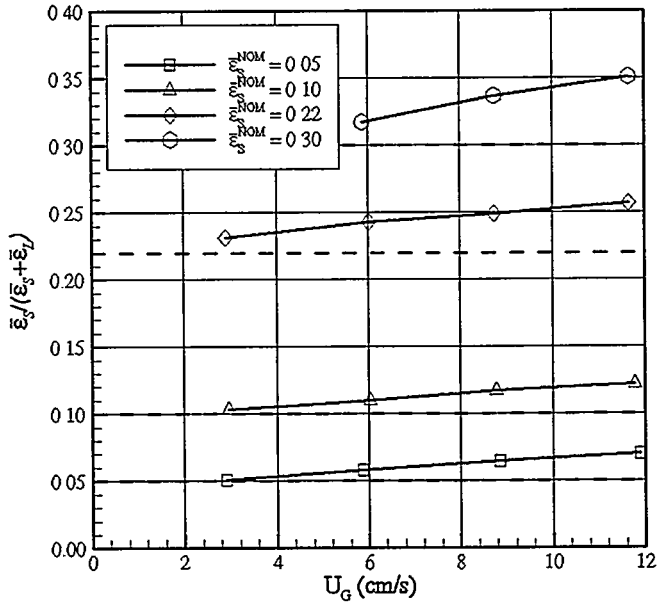

Figure 5.16. Dependence of the ratio $\bar{\varepsilon}_S/(\bar{\varepsilon}_S + \bar{\varepsilon}_L)$ on superficial gas velocity, calculated using the original Maxwell-Hewitt relation. The dashed lines indicate values of $\bar{\varepsilon}_S^{NOM}$ for each solids loading, the values that would be achieved if the solid were uniformly distributed in the liquid.

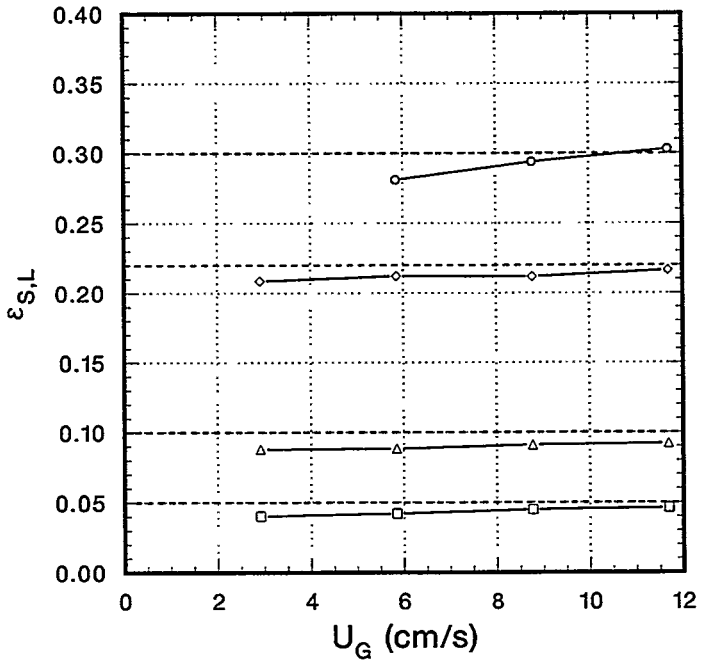

Figure 5.17. Dependence of the ratio $\bar{\varepsilon}_S/(\bar{\varepsilon}_S + \bar{\varepsilon}_L)$ on superficial gas velocity, calculated using the modified Maxwell-Hewitt relation.